Resonant coupling of dielectric optical waveguides
via rectangular microcavities: The coupled guided mode perspective

Manfred Hammer*

MESA$^+$ Research Institute, University of Twente, Enschede, The Netherlands

Abstract: Placed between two waveguides that serve as input and output ports, a wide segment of a third high contrast multimode dielectric waveguide can constitute the cavity in an integrated optical microresonator. We consider these devices in a spatial 2D setting by means of a bidirectional coupled mode theory (CMT) based on the guided fixed-frequency modes of the two port waveguides and the cavity segment. Combined with the numerically computed reflectivity of the cavity facets, the CMT equations can be solved for the power transmission of the resonators, in good agreement with rigorous mode expansion simulations. The CMT model allows to virtually detach the cavity from the port waveguides. Resonant configurations can thus be found as singularities in the matrix denominator of the CMT equations. Inspired by the field shape and the quality of some of the resonances, a more detailed look at the cavity facets reveals an effect of almost total reflection for specific slab mode superpositions. Both results together show that a slab waveguide mode solver is in principle sufficient for an approximate identification and classification of the resonances in the rectangular cavities. Several numerical examples illustrate the design procedure.

Keywords: integrated optics, numerical modeling, coupled mode theory, optical microresonators, rectangular microcavities

PACS codes: 42.82.–m 42.82.Et

1   Introduction

Applications in optical wavelength division multiplexing are a major objective of the current research efforts directed towards compact, highly integrated optical devices. Some promising concepts rely on microresonator elements as basic building blocks [1, 2], where, for reasons of size, the emphasis is on strongly guiding structures with high refractive index contrasts. In a typical resonator element, a small optical cavity is placed between two parallel straight waveguides that serve as input and output ports. The characteristic spectral response enables the design of microresonator devices with a variety of different prospective functionalities, e.g. for purposes of filtering, switching, routing, or modulation (see e.g. [1, 3, 4] and references cited therein).

While traditionally most investigations deal with cylindrical [5, 6, 7, 8, 9, 10, 1, 11, 3, 4] or elliptical [12, 13] cavity geometries, configurations with square or rectangular cavity shapes have attracted some interest as well. Recent studies consider the rectangular microresonators by means of a time domain coupled mode theory fitted to finite difference time domain calculations [14], by means of numerically rigorous analytical regularizations of contour integral equations [15], or alternatively by means of a frequency domain bidirectional mode expansion technique [16], where all investigations are restricted to a spatial twodimensional setting. Despite their rigorousness, these approaches give unfortunately only little insight in the design principles for the rectangular microcavities.

Tempted by the apparent resemblance with common three-core directional couplers [17, 18, 19] or radiatively coupled waveguides [20, 21], we propose to apply a coupled mode theory [22, 23] to the resonator device, based on the guided frequency domain modes supported by the port waveguides and by the cavity segment. The formulation resembles that given in Ref. [21] for the unidirectional light propagation along a three waveguide coupler. Aiming at the simulation of resonance phenomena, forward and backward traveling versions of the coupled fields have to be considered simultaneously. Combined with the numerically computed guided wave reflectivity of the cavity end facets [24], the coupled mode equations for both propagation directions allow to evaluate the power transmission of the resonator device. This is the subject of Section 3 of this paper.

---

*Faculty of Mathematical Sciences, University of Twente   *P.O. Box 217, 7500 AE Enschede, The Netherlands*
Phone: +31/53/489-3448   *Fax: +31/53/489-4833*   *E-mail: m.hammer@math.utwente.nl*

In particular, the coupled mode model allows to consider the cavity separated from the port waveguides. Resonant wavelengths and field patterns of the dielectric rectangles can thus be identified as singularities in the matrix denominator of the coupled mode equations. We evaluate this aspect in Section 4. The observations motivate a close look in Section 5 at the multimode waveguide facets that terminate the microresonator cavities. If one accepts the slab mode representation of the fields inside the cavities, this viewpoint leads directly to simple design guidelines for constructing cavities that support specific resonances at a prescribed frequency. Section 6 is concerned with this (approximate) reasoning. Examples for resonant configurations determined in this way can be found in Section 7.

2 Rectangular microcavities

Figure 1 sketches the resonator configuration. We restrict the problem to two spatial dimensions x, z, and to TE polarization, where only the single y-oriented component $\mathcal{E}_y$ of the electric field is present. All simulations in this paper are meant for light with constant angular frequency $\omega = k\mathrm{c} = 2\pi\mathrm{c}/\lambda$, given by the vacuum wavenumber k, the vacuum speed of light c, and the vacuum wavelength λ.
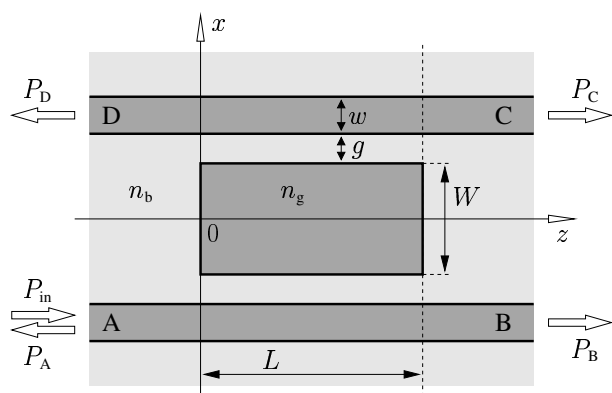

Figure 1: The microresonator geometry. Two identical waveguides of width w are placed a distance g apart from the rectangular cavity of length L and width W. The guiding regions with refractive index n_g, the waveguide cores and the cavity, are embedded in a background medium with refractive index n_b. Capital letters A to D denote the input respectively output ports of the device.

The rectangular, segmented structures can be simulated quite accurately and efficiently by mode expansion methods (bidirectional eigenmode propagation techniques) [22, 25], where we refer to Refs. [26, 16] for details of the present implementation. These simulations are rigorous up to convergence with respect to the extension of the computational window and with respect to the density of the spectral discretization, where forward and backward traveling, radiated and guided parts of the optical fields are taken fully into account. Calculations of that kind serve as a numerical reference for the more approximate discussion in this paper; all field plots included below are results from the rigorous model.
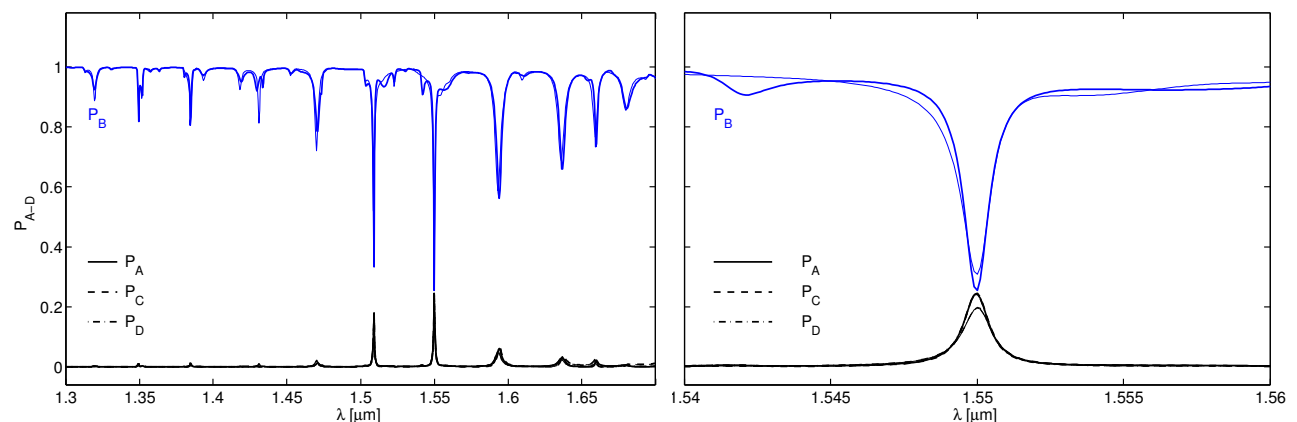

Figure 2: Wavelength response of a resonator device according to Figure 1 with dimensions $L = 5.738\,\mu m$, $W = 2.524\,\mu m$, $g = 0.450\,\mu m$, $w = 0.112\,\mu m$ for refractive indices $n_b = 1.45$ and $n_g = 3.40$ (see the first row of Table 1). P_A to P_D are the relative power fractions that are reflected respectively transmitted into ports A to D. The bold curves show the results of rigorous mode expansion simulations [16]; the thin lines, partially shadowed in the left inset, were computed according to Eqs. (13) by means of the coupled mode theory sketched in the following section.

2

Figure 2 shows a spectral response predicted in this way by a series of calculations with varying vacuum wavelength, for a specific resonator geometry with a relatively large, rectangular cavity. The device is excited in port A by the normalized, right-traveling guided mode of the lower core. For most wavelengths the input power is directly transmitted to port B, apart from a small power fraction lost to radiation. Resonant states appear as a drop in the direct transmission P_B and a simultaneous increase in the relative power fractions P_A, P_C, and P_D, that are reflected into port A, or dropped into ports C and D, respectively, where the three curves related to P_A, P_C, and P_D coincide almost completely.

The structure has been optimized for the resonance at $\lambda = 1.55 \, \mu m$, magnified in the right part of Figure 2. At resonance one observes relative power transmissions of $P_A = 24.4\%$, $P_B = 25.5\%$, $P_C = 24.5\%$, and $P_D = 24.2\%$, i.e. the unit input power is nearly equally distributed among the four output ports. The corresponding resonant field profile in Figure 3 shows outwards traveling guided waves in ports B, C, and D. The field in port A is a partly traveling, partly standing wave, the superposition of the unit input and the reflection with quarter amplitude. Inside the cavity, a purely standing wave pattern appears, with an extremal shape as plotted.
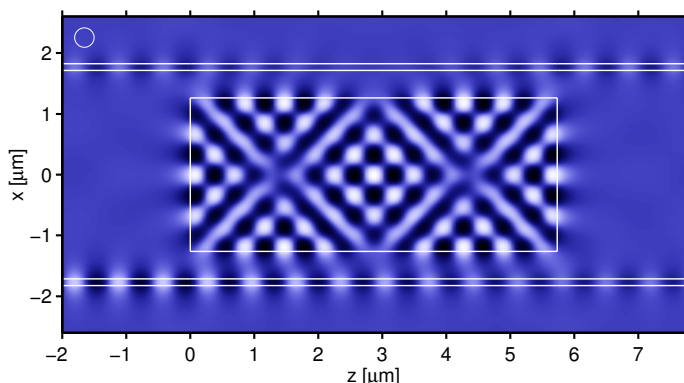

Figure 3: Field pattern for the pronounced resonance in Figures 2, 4. The plot shows the real optical electric field at a time position where the field inside the cavity is extremal. White and black regions indicate positive and negative field strength; the gray background marks the zero level.

While similar features and their prospective application for wavelength filter devices are described in much more detail in Refs. [14, 16], the numerical techniques used in those investigations provide hardly any means to classify and to predict the rather irregularly appearing resonances visible in Figure 2. Therefore in the following section we reconsider the structures in terms of an approximate, lower dimensional perturbational model.

3   Coupled mode theory modeling

The cavity region $0 < z < L$ of the microresonator can be regarded as a segment of length L of a symmetrical conventional directional coupler, constituted by the three parallel cores of the port waveguides and the cavity. We apply a corresponding coupled mode formalism [21] to describe the unidirectional guided light propagation along the cavity segment. Starting point are the guided modes related to the symmetric slab waveguides of thicknesses w and W that constitute the ports and the cavity of the device. The basis fields are given by the electric part $\boldsymbol{E}_m = (0, E_{m,y}, 0)$ and the magnetic part $\boldsymbol{H}_m = (H_{m,x}, 0, iH_{m,z})$ of the TE mode profiles, and by the corresponding (positive) propagation constants β_m, where $E_{m,y}$, $H_{m,x}$, and $H_{m,z}$ are real quantities. Using common complex notation, the forward propagating optical electromagnetic field at time t in the cavity segment is then assumed to be a superposition

$$\begin{pmatrix} \mathcal{E} \\ \mathcal{H} \end{pmatrix}(x, z, t) = \sum_m F_m(z) \frac{1}{\sqrt{P_m}} \begin{pmatrix} \boldsymbol{E}_m \\ \boldsymbol{H}_m \end{pmatrix}(x) \exp(i\omega t) \tag{1}$$

of the single modes, normalized by $P_m = -\int E_{m,y} H_{m,x} \, dx/2$, with coefficients F_m which include the harmonic dependence on the propagation distance. Each mode is assigned the difference $\Delta \epsilon_m = \epsilon - \epsilon_m$ between the permittivity profile ϵ that describes the entire three guide structure and the permittivity ϵ_m of the single slab structure for which the mode was calculated.

Then a reasoning by means of reciprocity techniques [22, 21] leads to the following coupled mode equations, written directly in matrix form for the vector $\boldsymbol{F} = (F_m)$ of forward mode amplitudes:

$$\mathsf{S}\partial_z \boldsymbol{F} = -\mathrm{i}(\mathsf{Q} + \mathsf{K})\boldsymbol{F}\,. \tag{2}$$

The real symmetric matrices $\mathsf{S} = (\sigma_{lm})$ (positive) and $\mathsf{Q} = (\sigma_{lm}(\beta_l + \beta_m)/2)$ collect the power coupling coefficients

$$\sigma_{lm} = \frac{-1}{4\sqrt{P_l P_m}} \int (E_{l,y} H_{m,x} + E_{m,y} H_{l,x})\,\mathrm{d}x \tag{3}$$

and propagation constant averages, respectively, while for lossless materials $\mathsf{K} = (\kappa_{lm})$ is the Hermitian matrix of coupling coefficients

$$\kappa_{lm} = \frac{\omega\epsilon_0}{8\sqrt{P_l P_m}} \int \boldsymbol{E}_l^* (\Delta\epsilon_l + \Delta\epsilon_m)\boldsymbol{E}_m\,\mathrm{d}x\,. \tag{4}$$

The coupled mode equations (2) are readily solved by an exponential ansatz

$$\boldsymbol{F}(z) = \sum_s f^s \frac{1}{\sqrt{P^s}}\boldsymbol{a}^s \exp(-\mathrm{i}\beta^s z)\,, \tag{5}$$

where $\boldsymbol{a}^s$ and β^s are the constant amplitude vectors and phase constants that describe the so-called supermodes of the structure, normalized by $P^s = (\boldsymbol{a}^s)^\mathsf{T}\mathsf{S}\boldsymbol{a}^s$, superimposed with coefficients f^s. Being the (real) solutions of the generalized eigenvalue problem

$$(\mathsf{Q} + \mathsf{K})\boldsymbol{a}^s = \beta^s \mathsf{S}\boldsymbol{a}^s\,, \tag{6}$$

the supermode vectors satisfy the orthogonality properties $(\boldsymbol{a}^r)^\mathsf{T}\mathsf{S}\boldsymbol{a}^s = \delta_{rs}P^s$. Here $^\mathsf{T}$ denotes the transpose, $\delta_{rr} = 1$, and $\delta_{sr} = 0$ if $r \neq s$. Projection on a given initial amplitude vector $\boldsymbol{F}(0)$ yields the expansion coefficients $f^s = (1/\sqrt{P^s})(\boldsymbol{a}^s)^\mathsf{T}\mathsf{S}\boldsymbol{F}(0)$, such that the general solution of Eq. (2) for the forward propagation along the entire cavity segment $0 < z < L$ can be written as

$$\boldsymbol{F}(L) = \mathsf{T}(L)\boldsymbol{F}(0) \tag{7}$$

with

$$\mathsf{T}(L) = \Big(\sum_s \frac{1}{P^s} \exp(-\mathrm{i}\beta^s L)\boldsymbol{a}^s(\boldsymbol{a}^s)^\mathsf{T}\Big)\mathsf{S}\,. \tag{8}$$

Details on the only briefly sketched derivation above and on related issues can be found in Ref. [21].

A completely analogous reasoning holds for the backward light propagation, based on the backwards traveling versions of the guided mode profiles of the three cores and the corresponding negative propagation constants. The propagation matrix $\mathsf{T}(L)$ as defined in (8) relates the backward mode amplitudes $\boldsymbol{B}$ at the beginning $z = 0$ of the cavity segment to the amplitudes at $z = L$ as

$$\boldsymbol{B}(0) = \mathsf{T}(L)\boldsymbol{B}(L)\,. \tag{9}$$

With the descriptions of the bidirectional guided light propagation along the cavity segment at hand, the next step towards a model for the microresonator device is to separate the modes in the port channels from the fields in the cavity waveguide. Therefore we split the amplitude vectors $\boldsymbol{F}$ and $\boldsymbol{B}$ and the propagation matrix as

$$\boldsymbol{F} = \begin{pmatrix} \boldsymbol{F}_\mathrm{p} \\ \boldsymbol{F}_\mathrm{c} \end{pmatrix}, \quad \boldsymbol{B} = \begin{pmatrix} \boldsymbol{B}_\mathrm{p} \\ \boldsymbol{B}_\mathrm{c} \end{pmatrix}, \quad \mathsf{T} = \begin{pmatrix} \mathsf{T}_\mathrm{pp} & \mathsf{T}_\mathrm{pc} \\ \mathsf{T}_\mathrm{cp} & \mathsf{T}_\mathrm{cc} \end{pmatrix}, \tag{10}$$

4

where the indices p and c indicate port and cavity related entries. Now $\boldsymbol{F}_\mathrm{p}(0)$ and $\boldsymbol{B}_\mathrm{p}(L)$ can be regarded as the input to the device, $\boldsymbol{F}_\mathrm{p}(L)$ and $\boldsymbol{B}_\mathrm{p}(0)$ are the amplitudes of the output fields.

To complete the resonator model, the cavity mode amplitudes $\boldsymbol{F}_\mathrm{c}$ and $\boldsymbol{B}_\mathrm{c}$ are to be related at the positions $z = 0$ and $z = L$ of the facets of the cavity waveguide. Neglecting completely the presence of the port cores as a — rough — approximation when handling the cavity facet problem, we apply the mode expansion technique [26, 16] mentioned in Section 2 to the facet structure constituted by a semi-infinite segment of the isolated cavity waveguide. These simulations consider rigorously the optical fields around the facet, including the transmitted and reflected radiation. Restricted to the guided incident and reflected modes in the core layer, the results establish linear relations

$$\boldsymbol{B}_\mathrm{c}(L) = \mathsf{R}\boldsymbol{F}_\mathrm{c}(L), \quad \boldsymbol{F}_\mathrm{c}(0) = \mathsf{R}\boldsymbol{B}_\mathrm{c}(0), \tag{11}$$

between the mode amplitudes involved in the two independent identical facet problems at $z = 0$ and $z = L$, with a complex, nonunitary, symmetric reflectivity matrix R (cf. Ref. [24]).

The total guided optical power, the integrated z-component of the pointing vector, associated with a field superposition (1) is $\boldsymbol{F}^\dagger \mathsf{S} \boldsymbol{F}$, where † denotes the adjoint. The propagation matrix $\mathsf{T}(L)$ conserves this quantity: $(\mathsf{T}(L))^\dagger \mathsf{S} \mathsf{T}(L) = \mathsf{S}$. Being perfectly adequate if one remains in the in the framework of the coupled mode description with nonorthogonal basis fields, this implies that $\mathsf{T}(L)$ is a nonunitary matrix. But to connect the description (10) of the propagation along the cavity segment and the facet model (11), one has to leave that framework. The mode amplitudes are viewed as belonging to two separate problems, each including a set of pairwise orthogonal basis fields (either because of the distance between the cores, or because of the exact orthogonality of modes in the same multimode core), and consequently the total power is to be evaluated as the absolute square $\boldsymbol{F}^\dagger \boldsymbol{F}$ of the mode amplitude vectors. Power conservation for the amplitude transfer between $z = 0$ and $z = L$ in this setting requires $\mathsf{T}(L)$ to be unitary.

Splitting the power coupling matrix as $\mathsf{S} = \mathsf{X}^\mathsf{T} \mathsf{X}$, the matrix $\mathsf{X} \mathsf{T} \mathsf{X}^{-1}$, with T as in Eq. (8), has the desired property. Therefore we redefine the propagation matrix and accordingly Eqs. (7), (9), and (10) in a symmetrized form as

$$\mathsf{T}(L) = \mathsf{X}\Big(\sum_s \frac{1}{P^s} \exp(-\mathrm{i}\beta^s L) \boldsymbol{a}^s (\boldsymbol{a}^s)^\mathsf{T} \Big) \mathsf{X}^\mathsf{T}, \tag{12}$$

where X^T and X are the factors of the Cholesky decomposition of S, that are actually already used to solve Eq. (6). Being a direct consequence of the approximations inherent in the coupled mode ansatz (1) and in the change of viewpoints (10), this inconsistency leads to realistic, non-amplified power transmission curves (Note that the difficulty does not show up, if the offdiagonal power coupling coefficients are a priori neglected as in many coupled mode theory formulations).

Now the independent expressions (7), (9), (10) for the propagation along the cavity segment and (11) for the reflection at the facet can be combined, where due to the symmetry of the linear device it is sufficient to consider an input from one side only. In case of an excitation $\boldsymbol{F}_\mathrm{p}(0)$ from the left and no incoming field from the right $\boldsymbol{B}_\mathrm{p}(L) = 0$, one obtains

$$\boldsymbol{F}_\mathrm{p}(L) = (\mathsf{T}_\mathrm{pp} + \mathsf{T}_\mathrm{pc} \mathsf{R} \Omega^{-1} \mathsf{T}_\mathrm{cc} \mathsf{R} \mathsf{T}_\mathrm{cp}) \boldsymbol{F}_\mathrm{p}(0), \quad \boldsymbol{B}_\mathrm{p}(0) = \mathsf{T}_\mathrm{pc} \mathsf{R} \Omega^{-1} \mathsf{T}_\mathrm{cp} \boldsymbol{F}_\mathrm{p}(0) \tag{13}$$

for the transmission through the device and for the reflections caused by the resonator, while the field inside the cavity is given by

$$\boldsymbol{F}_\mathrm{c}(L) = \Omega^{-1} \mathsf{T}_\mathrm{cp} \boldsymbol{F}_\mathrm{p}(0), \quad \boldsymbol{B}_\mathrm{c}(0) = \Omega^{-1} \mathsf{T}_\mathrm{cc} \mathsf{R} \mathsf{T}_\mathrm{cp} \boldsymbol{F}_\mathrm{p}(0). \tag{14}$$

All expressions are governed by a resonance denominator in matrix form

$$\Omega = 1 - \mathsf{T}_\mathrm{cc} \mathsf{R} \mathsf{T}_\mathrm{cc} \mathsf{R}. \tag{15}$$

5

Besides the resonance related matrices, the expression (13) for $\boldsymbol{F}_{\mathrm{p}}(L)$ contains a first term that is independent from the reflectivity matrix. Representing the direct coupling in standard coupler models (see Refs. [17, 18, 19] or [20, 21]), for the present short, weakly coupled structures the effect is a slight asymmetry in the forward and backward drop and a small traveling wave contribution to the field inside the cavity with a slow wavelength dependence. Hence here we do not pay special attention to this nonresonant mechanism, though it is included in all simulations of complete resonators.

Assigning indices 1 and 2 to the modes of the lower and upper port waveguides, respectively, for an input in port A represented by $\boldsymbol{F}_{\mathrm{p}}(0) = (\sqrt{P_{\mathrm{in}}}, 0)^{\mathsf{T}}$, the coupled mode model predicts

$$P_{\mathrm{A}} = |B_{\mathrm{p},1}(0)|^2/P_{\mathrm{in}}, \quad P_{\mathrm{B}} = |F_{\mathrm{p},1}(L)|^2/P_{\mathrm{in}}, \quad P_{\mathrm{C}} = |F_{\mathrm{p},2}(L)|^2/P_{\mathrm{in}}, \quad P_{\mathrm{D}} = |B_{\mathrm{p},2}(0)|^2/P_{\mathrm{in}} \qquad (16)$$

for the relative amounts of reflected, directly transmitted, and forwards and backwards dropped optical power.

Figures 2 and 4 compare transmission curves that are computed by means of this approximate model with the results of rigorous simulations. Regarding the quite adverse conditions for the application of coupled mode theory — the high refractive index contrast, and the long (unfolded) interaction length — the agreement is reasonable. Obviously the field inside the cavity can be represented well by a bidirectional version of the superposition (1) of guided modes in the corresponding slab waveguide.

4   Multimode resonances

Resonant configurations are distinguished by an abrupt raise or drop in the power transmission, and by a singular high field intensity inside the cavity [16]. In the products of matrices in Eqs. (13), (14), the term Ω^{-1} is the only common factor that is likely to be responsible for that phenomenon.

Considering e.g. the expression (14) for the amplitudes $\boldsymbol{F}_{\mathrm{c}}(L)$ at the end of the cavity, a huge intensity requires that a field is excited there — the input $\boldsymbol{F}_{\mathrm{p}}(0)$ mapped by T_{cp} — that is significantly amplified by the term Ω^{-1}. This holds for an amplitude vector $\boldsymbol{v}$ that corresponds to a large (in terms of absolute value) complex eigenvalue a of Ω^{-1}; the cavity then amplifies the intensity according to $|\Omega^{-1}\boldsymbol{v}|^2 = |a|^2|\boldsymbol{v}|^2$ by a factor $A = |a|^2$. For a fixed cavity configuration, the maximum amplification is given by the largest eigenvalue a of Ω^{-1}, alternatively by the smallest eigenvalue $1/a$ of Ω, or by the eigenvalue $1 - 1/a$ of $\mathsf{T}_{\mathrm{cc}}\mathsf{R}\mathsf{T}_{\mathrm{cc}}\mathsf{R}$ that is closest to 1. This last characterization allows a quite descriptive interpretation: In a resonant state, a field is excited at the end of the cavity, that is exactly reproduced after being reflected once at the cavity facet, being propagated backwards through the cavity, being reflected a second time, and being transferred forwards to its original position.

Writing the eigenvalue $r\exp(\mathrm{i}\varphi)$ of $\mathsf{T}_{\mathrm{cc}}\mathsf{R}$ that is nearest to -1 or $+1$ in terms of its absolute value r and its argument φ, the amplification factor A reads

$$A = \frac{1}{1 + r^4 - 2r^2\cos(2\varphi)}. \qquad (17)$$

A is defined in terms of R and T_{cc}. While the former is by construction a property of the isolated cavity, the latter becomes a property of the cavity only, if the port waveguides are removed: In the limit of a large gap width $g \to \infty$, the cavity propagation matrix assumes the diagonal form $\mathsf{T}_{\mathrm{cc}} \to \mathrm{diag}(\exp(-\mathrm{i}\beta_m L))$, where the diagonal elements are the phase factors corresponding to the propagation of the modes of the cavity waveguide. Consequently, in the limit of absent port waveguides, the evaluation of the amplification factors yields a quantitative characterization of the resonances in a 2D dielectric rectangle. This reasoning naturally leads to considering the cavity length L as a tuning parameter, for fixed vacuum wavelength of the input light. Figure 4 shows the corresponding dependences, including the pronounced resonance from Figure 2.

Applied to the description of an entire resonator device, this viewpoint obviously disregards the influence of the port waveguides completely. Nevertheless one can expect that the cavity properties dominate the position of the peaks observed in the power transmission of the device, with only a minor perturbation due to the presence of the ports. Simultaneously, the port waveguide configuration determines the strength of the excitation, or whether a resonance appears at all. These notions are justified by the numerical experiments of Ref. [16], but also by the coincidences of the peak positions in the curves of Figure 4.

With the coefficients of R being only numerically defined, in general (17) does not permit an explicit analytical evaluation, if all guided modes of the cavity waveguide are included (in the examples of Figures 2–4 these are 11 basis fields). Assuming, however, that only a single mode plays a dominant role, the matrices reduce to scalar quantities $\mathsf{T} = \exp(-i\beta_m L)$ and $\mathsf{R} = r_m \exp(i\psi_m)$ given by the propagation constant β_m of the relevant cavity mode and by the related entry of the facet reflectivity matrix with absolute value r_m and phase $\exp(i\psi_m)$. The corresponding amplification factor reads

$$A_m = \frac{1}{1 + r_m^4 - 2r_m^2 \cos(2\psi - 2\beta_m L)} \, . \tag{18}$$

Consequently, cavities with lengths $(\psi + j\pi)/\beta_m$, for natural j, should support a resonance related to cavity mode m, where the quality is determined by the relative amount of power r_m^2, that is reflected back into that mode at the facets.
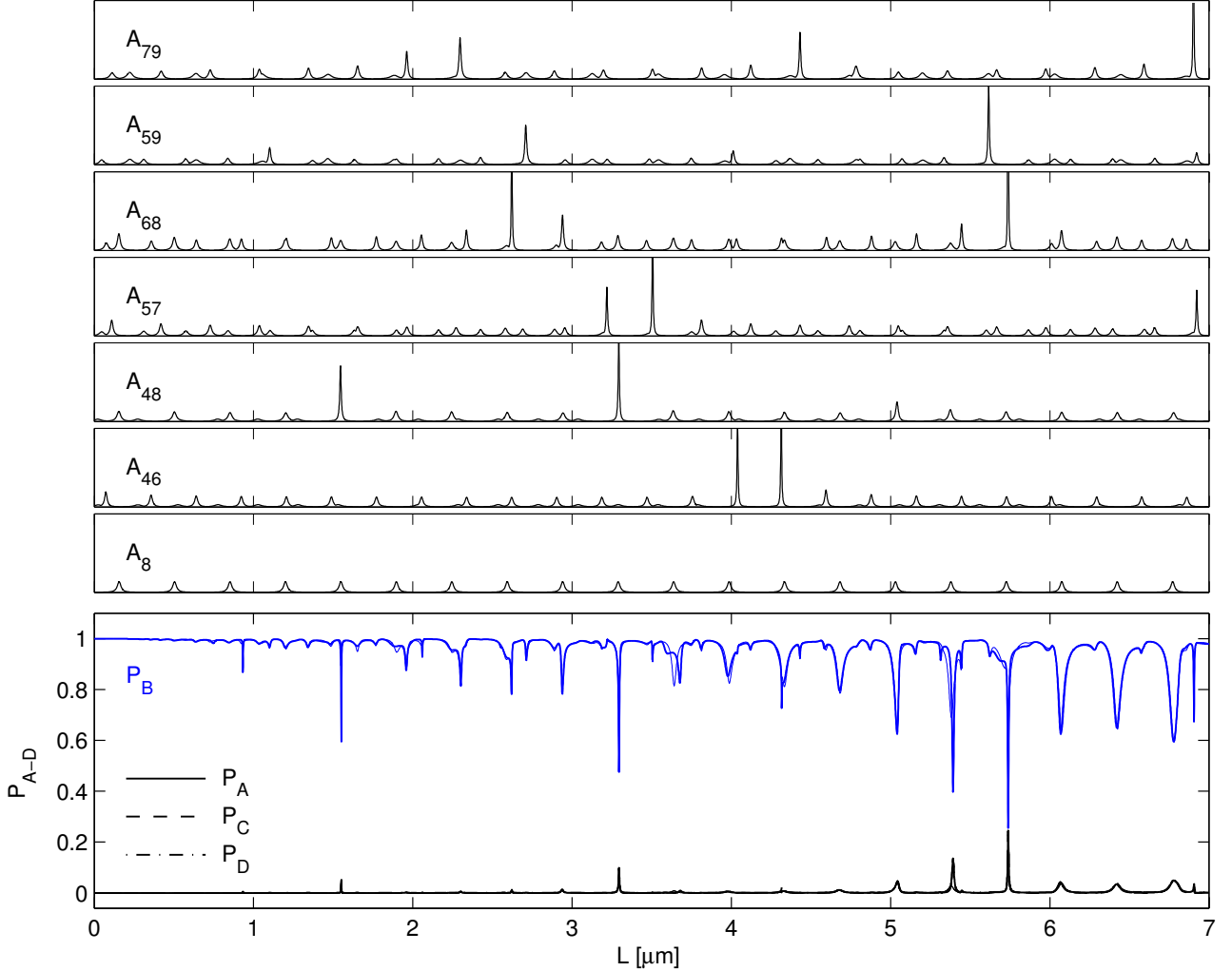

Figure 4: Bottom: Power transmission through a device according to Figure 1 versus the cavity length L. Geometrical parameters are $W = 2.524\,\mu m$, $g = 0.450\,\mu m$, $w = 0.112\,\mu m$; the vacuum wavelength is kept at $\lambda = 1.55\,\mu m$. Thick and thin curves correspond to the rigorous and coupled mode resonator models. Top: Amplification factors (17) and (18) related to the characteristic resonance denominators (15) of the isolated cavities. A_{lm} and A_m are restrictions of Eq. (17) to the modes of order $l, m,$ and m, respectively. See the text for a concise interpretation of these curves.

Figure 4 includes a plot of the amplification factor A_8 for the 8-th order cavity mode. In the full resonator simulations the port configuration was designed such that the individual port waveguides are phase matched with that cavity mode. Clearly resonances are excited regularly at the lengths predicted by Eq. (18), where the amount of power that is dropped, reflected, or lost, respectively, depends on the precise excitation conditions, i.e. grows with the interaction length. Two examples of field profiles for these single mode resonances in Figure 12 exhibit the expected regular standing wave patterns with 8 horizontal nodal lindes inside the cavity, surrounded by a relatively large amount of radiation.

7

Due to the specific tailoring of excitation conditions, among the 11 guided fields the single mode resonances related to the 8-th order mode are the dominant ones. Apart from these, several other peaks appear irregularly in the resonator spectrum of Figure 4, some of which are much narrower and much more pronounced. An extraordinary quality is also observed for the peaks located at a few of the single resonance positions, including the resonance emphasized in Figure 2. The related field patterns, exemplified by the plot in Figure 3, are not of the simple shape of Figure 12. Consequently, more than one cavity mode must be suspected to be relevant in these cases.

The curves labeled A_{lm} in Figure 4 indicate that a set of two guided cavity fields is sufficient to identify most of the resonances. The values A_{lm} are computed by restricting Eq. (17) to the two basis modes of order l and m. In the limit $g \to \infty$ the two modes propagate independently along the cavity, being connected via the reflection at the facets. Hence the amplification A_{lm} appears simply as the maximum of the factors A_l and A_m related to the individual modes if at a length L the phase relation for single mode resonances is satisfied for only one of the two modes. The regular features of $A_4 - A_9$ can thus be found in the curves for $A_{46} - A_{79}$ in Figure 4.

If, however, proper phase relations are met for both modes simultaneously, much more pronounced resonances can occur. This requires a mechanism that yields a significantly higher guided wave reflectivity, compared to single mode incidence, if superpositions with specific relative amplitude of two cavity modes are incident on the facets. The pronounced bimodal resonances in A_{lm} are located where the single mode peaks in A_l and A_m pass over each other with growing L, provided the individual peaks approach sufficiently, where only for some of these lengths a pronounced resonance shows up. Apparently, a specific relative phase relation of the incident fields is required for a high bimodal reflectivity, a condition which is not satisfied for all of the lengths indicated by the approaching peaks in A_l and A_m.

Being eigenfunctons of a symmetric slab structure, the basis modes in the cavity waveguide have a definite symmetry. Reflection at the cavity facets preserves that symmetry, i.e. the offdiagonal coefficients in the reflectivity matrix related to modes of different symmetry vanish. Hence the amplification factors A_{lm} for an even mode order l and an odd order m (not shown in Figure 4) are just the maxima of the two single mode curves A_l and A_m; only modes with equal symmetry can establish a bimodal resonance.

5 Multimode reflection at the cavity facets

For an explanation of the high reflectivity effect predicted in the last section a reasoning in terms of the familiar ray picture for guided wave propagation in a dielectric slab is helpful. According to Figure 5, the mode angle θ associated with a mode with propapagtion constant $\beta = k n_g \cos \theta$ can alternatively be regarded as the incidence angle of the corresponding waves on the facet interface.
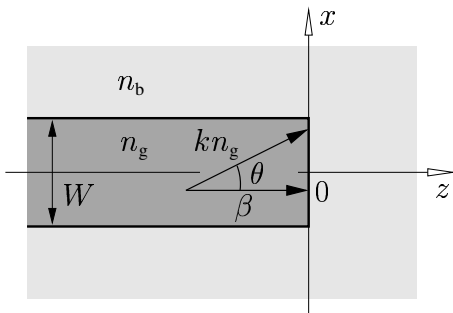
Figure 5: A facet of the waveguide that forms the cavity of the microresonator in Figure 1. A propagation constant β and a mode angle θ are assigned to each guided mode.

Consequently, in this framework a high reflectivity can be expected for an individual mode, if its angle is larger than the critical angle θ_{crit} for total reflection at an interface between two dielectrica with refractive indices n_g and n_b, given by $\sin \theta_{crit} = n_b / n_g$. Figure 6 shows rigorous results for the relative power reflected back into specific sets of incidence modes for the fields relevant in the configurations of Figures 3–4 and 12.

The single mode reflectivities indeed meet the expectations. The fundamental and low order modes with small mode angles are subject to small reflectivities just above the level $(n_g - n_b)^2 / (n_g + n_b)^2$ for the reflection of a perpendicularly incident plane wave. The single mode reflectivity raises for modes with angles around θ_{crit} and
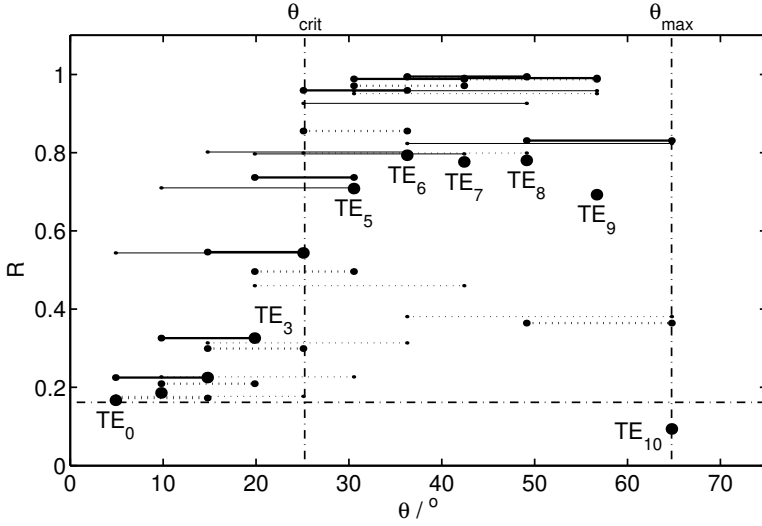
Figure 6: Reflectivities R of single modes (filled circles) and of two mode superpositions (bars) versus the discrete mode angle, for a waveguide facet with the parameters of the cavity of Figure 3. Continuous and dotted bars correspond to superpositions of the two fields with angles at the end points, where the input amplitudes are determined such that the reflectivity is maximum, or such that the optical electric field vanishes at the facet edges, respectively.

larger, and drops again for the highest order modes with angles close to the maximum value $\cos\theta_{max} = n_b/n_g$, where a major part of the profile exists in the background medium $|x| > W/2$, i.e. does not feel the facet interface. But even for the intermediate fields of order 6, 7, 8, with a reflectivity of about 80% the reflection is by no means total.

This changes drastically, if one considers superpositions of two incident modes with $\theta > \theta_{crit}$ with equal symmetry. The continuous bars in Figure 6 mark the maximum reflectivity levels for a linear combination of the two modes indicated by the bar ends. The simulation predicts a highest value of 99.4% for the modes TE_6 and TE_8, with the difference to full reflection being almost beyond the accuracy that can be expected from the numerical computations.

The origin of this effect is revealed by the field patterns in Figure 7. For incidence of the individual modes TE_6 and TE_8, one observes mainly standing waves inside the core, exponential mode tails at the upper and lower waveguide interface, and a similar field decay across the facet. The radiation outside the core appears as two cylindrical waves, originating from the edges in the facet plane. If the relative amplitude and phase of the two modes are adjusted such that their superposition vanishes in these points, the cylindrical waves found for the single mode incidences interfere destructively; almost the entire incident power is reflected into the two guided fields. The very high reflectivity level of 99.3% achieved with this adjustment of input amplitudes, and the agreement of the resulting field profile with the standing wave pattern inside the microresonator cavity in Figure 3 indicates that this is indeed the mechanism that enables the bimodal resonances.
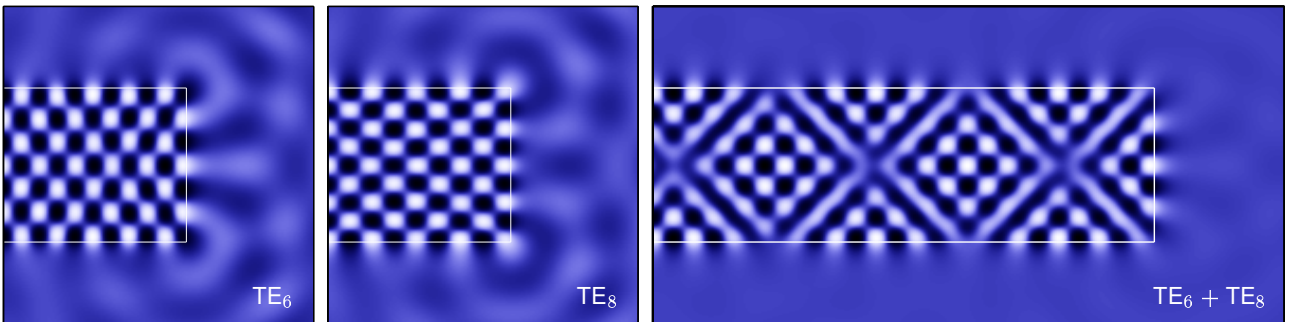

Figure 7: Extremal field profiles around the facet of a multimode waveguide with the parameters of the cavity of Figure 3, for an excitation by individual modes of order 6 (left) and 8 (center), and for a specific superposition of these two incoming fields (right).

Similar series of high contrast multimode waveguide facets have been investigated in Ref. [24], where explicit expressions for the relevant mode amplitudes are given, that lead to the total reflection effect. Apparently, these amplitudes establish themselves automatically in case of the rectangular cavity resonances.

The results above complement the findings concerning the amplification factors in Section 4: Obviously the

destructive interference of the cylindrical waves is impossible, if the participating modes are of opposite symmetry with respect to $x = 0$. Compared to the reflectivity levels that can be achieved in the bimodal case, the moderate single mode reflectivities render the single mode resonances rather weak. A resonance requires the cavity length to match the propagation cycles, such that fields like the ones in the left and center plot of Figure 7 emerge around both cavity facets. At a bimodal resonance built from modes l and m, this condition is to be met for two modes simultaneously, hence peaks in A_l and A_m have to coincide. For destructive interference of the corresponding radiation, additionally equal symmetry with respect to the vertical plane $z = L/2$ is required. The signs of the field amplitudes related to mode l should match those related to mode m simultaneously at all four corner points of the cavity. Only in that case the amplification factor A_{lm} shows a peak higher than just the maximum of A_l and A_m.

6 Slab mode reasoning

Accepting the result of Section 4, that an approximation by slab waveguide modes is adequate for the field inside the cavity, we consider again an isolated dielectric rectangle as sketched in Figure 8. To facilitate symmetry arguments, the origin of the coordinate system is shifted to the center of the structure.
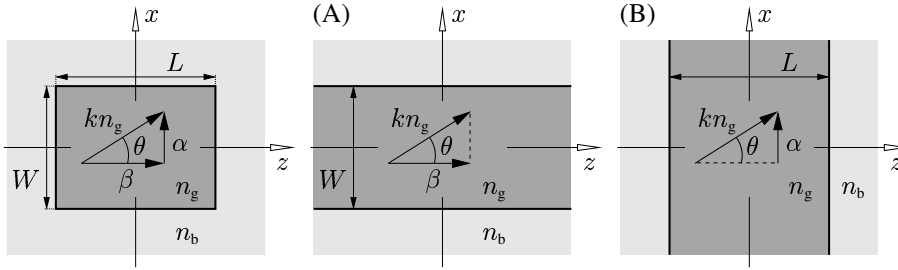

Figure 8: A rectangular cavity viewed as a finite segment of a horizontally (A) or vertically (B) oriented slab waveguide.

Apart from the time dependence and up to an arbitrary complex amplitude, the y-component of the electrical (TE) field E_y of a resonance corresponding to a single mode with profile φ and propagation constant β can be stated in the form

$$E_y(x, z) = \varphi(x)\left(e^{-i\beta z} + b\,e^{i\beta z}\right), \tag{19}$$

restricted to the segment $-L/2 < z < L/2$, where b is the relative amplitude of the backwards traveling part of the field. The mode profile φ is of a definite symmetry, with a harmonic x-dependence inside the cavity:

$$\varphi(x) = e^{-i\alpha x} \pm e^{i\alpha x}, \quad \text{for} \quad -W/2 < x < W/2 \quad \text{with} \quad \alpha = \sqrt{k^2 n_{\mathrm{g}}^2 - \beta^2}, \tag{20}$$

such that the field inside the cavity reads

$$E_y(x, z) = \left(e^{-i\alpha x} \pm e^{i\alpha x}\right)\left(e^{-i\beta z} + b\,e^{i\beta z}\right). \tag{21}$$

This corresponds to viewpoint (A) in Figure 8, where the cavity is regarded as a finite segment of length L of a horizontally oriented slab waveguide of thickness W. Obviously the setting (B), where the cavity is regarded as a segment of length W of a vertically oriented slab with thickness L, should be completely equivalent. Thus, if Eq. (21) is supposed to describe the field of a single mode resonance, it must be interpretable as a mode of the slab of thickness L, traveling in positive and negative x-direction.

Having exchanged the roles of x and z in this way, the symmetry condition with respect to $z = 0$ can be satisfied by requiring $b = \pm 1$, and one has to identify the second factor $\psi(z) = e^{-i\beta z} \pm e^{i\beta z}$ in Eq. (21) as the mode profile, corresponding to the propagation constant α. Here $\beta = kn_{\mathrm{g}} \cos\theta$ and $\alpha = kn_{\mathrm{g}} \cos(\pi/2 - \theta)$ are related via the mode angles θ and $\pi/2 - \theta$ associated with φ and ψ, respectively.

Consequently, one can expect that a single mode resonance can be excited inside a rectangular cavity with dimensions L and W, if simultaneously the planar symmetric slab waveguide of thickness W supports a guided
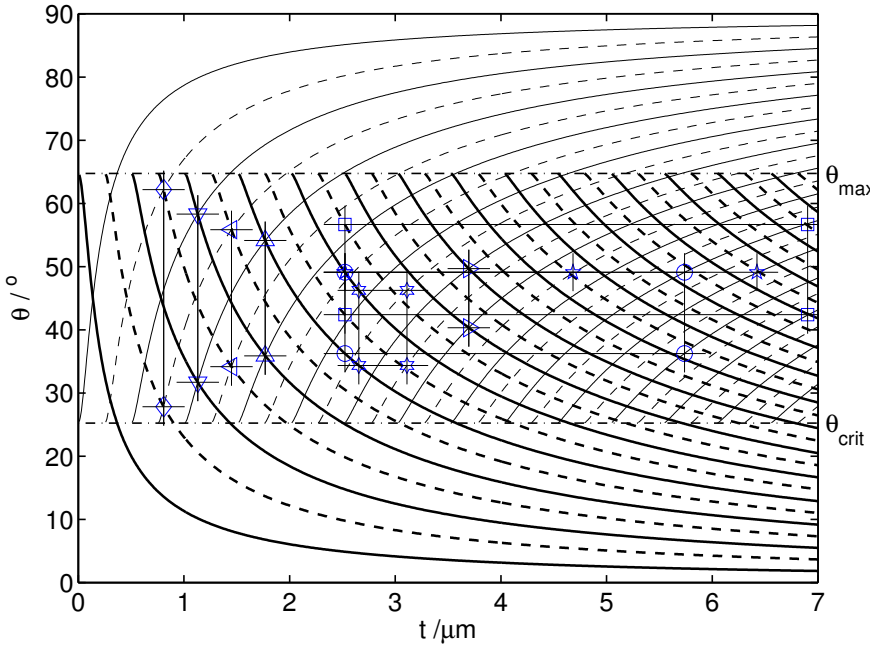
Figure 9: Angles θ (thick lines) associated with the guided modes of symmetric planar waveguides of thickness t and core / cladding refractive indices of $n_g = 3.40$ and $n_b = 1.45$ for TE polarized light with a vacuum wavelength of 1.55 μm; the thin curves are the levels $\pi/2 - \theta$. The upper horizontal line indicates the maximum admissible mode angle θ_{max}, the lower line is placed at the critical angle θ_{crit} for total reflection at a dielectic interface with refractive index contrast of $n_g | n_b$. The remaining marker symbols and the connecting lines correspond to the field patterns of Figures 3, 10, 11, and 12. See the text for a concise interpretation.

mode with mode angle θ_W, while the planar symmetric slab of thickness L supports a mode with angle $\theta_L = \pi/2 - \theta_W$. Resonant configurations can thus be constructed by considering a plot of the mode angles versus the slab waveguide thickness like Figure 9.

For a single mode resonance, one could start with a horizontal line at angle θ within the interval $\theta_{\mathrm{crit}} < \theta < \theta_{\mathrm{max}}$. Choosing an intersection point with a bold curve fixes one side length W of the cavity and the corresponding angle $\theta = \theta_W$. An intersection point with a thin curve yields the second cavity dimension L and the angle $\theta = \pi/2 - \theta_L$. In Figure 9, an example is marked by the symbol of configurations (8) and (9) from Table 1. Due to the harmonic dependence of the slab mode profiles on the transverse coordinate the $\theta(t)$ curves cross the horizontal lines at equidistant points: If the waveguide of thickness L supports a mode with angle θ_L, all waveguides with thicknesses $L \pm j\pi/(kn_g \cos(\pi/2 - \theta_L)) = L \pm j\pi/(kn_g \cos \theta_W)$, for integer j, support modes with the same angle. With $\beta = kn_g \cos \theta_W$, this corresponds directly to the periodically appearing single mode resonances in a plot of the transmission versus the cavity length (cf. Figure 4). Note that here the weak transition from low to high facet reflectivity around θ_{crit} (see Figure 6) becomes a well defined limit: Constructing a single mode resonance as outlined requires $\theta_L < \theta_{\mathrm{max}}$ and consequently $\theta_W = \pi/2 - \theta_L > \pi/2 - \theta_{\mathrm{max}} = \theta_{\mathrm{crit}}$.

An ansatz like (19) for a bidirectional superposition of two basis modes initiates an analogous reasoning for bimodal resonances. In this framework a bimodal resonance can be excited, if the slab waveguide of thickness W supports two modes with angles θ_1, θ_2, while simultaneously the slab of thickness L guides two modes with angles $\pi/2 - \theta_1, \pi/2 - \theta_2$. Defining $\beta_m = kn_g \cos \theta_m$, $\alpha_m = kn_g \cos(\pi/2 - \theta_m)$, the field associated with the pure standing wave inside the cavity is to be written

$$E_y(x, z) = (\mathrm{e}^{-\mathrm{i}\alpha_1 x} \pm \mathrm{e}^{\mathrm{i}\alpha_1 x})(\mathrm{e}^{-\mathrm{i}\beta_1 z} \pm \mathrm{e}^{\mathrm{i}\beta_1 z}) + a(\mathrm{e}^{-\mathrm{i}\alpha_2 x} \pm \mathrm{e}^{\mathrm{i}\alpha_2 x})(\mathrm{e}^{-\mathrm{i}\beta_2 z} \pm \mathrm{e}^{\mathrm{i}\beta_2 z}). \quad (22)$$

According to Section 5, a high quality resonance requires a zero field strength in the cavity corners. A field that vanishes simultaneously at all four corner points can indeed be realized by a properly established relative (real) amplitude a, provided that the the two 'horizontal' modes and at the same time the two 'vertical' modes involved are of equal symmetry.

Geometrical identification of configurations that are likely to exhibit bimodal resonances is straightforward for square cavities: One has to select a side length $L = W$, such that the slab with that thickness supports two modes of equal symmetry with mode angles θ_1 and $\theta_2 = \pi/2 - \theta_1$ in the range between θ_{crit} and θ_{max}. The examples in Figure 9 correspond to configurations (3) – (7) of Table 1. Identification of non-square rectangular cavities with bimodal resonances is more a matter of chance: Two constructions as sketched for the single mode resonances have to be matched such that they lead to the same dimensions L and W. Figure 9 indicates examples for the parameters of configurations (0), (1), (2) in Table 1.

The slab mode viewpoint leads immediately to a classification of the resonances in terms of the numbers of horizontal and vertical nodal lines in the involved basis fields. In Table 1 we use the notation $m_x \times m_z$ for single mode resonances and $m_x^1 \times m_z^1 + m_x^2 \times m_z^2$ for bimodal excitations, respectively. m_x and m_x^j are the orders of the modes with x-dependent profiles propagating along the z-axis, m_z and m_z^j are the numbers of nodes in the z-dependent profiles that propagate in the $\pm x$-direction.

A few constraints for the design of resonant configurations can be named directly. Basis modes must exist inside the cavity with angles $\theta_{\mathrm{crit}} < \theta < \theta_{\mathrm{max}}$. These are only supported by the equivalent cavity waveguides for a sufficient refractive index contrast $n_{\mathrm{g}} > \sqrt{2}\, n_{\mathrm{b}}$, where, for pronounced resonances, a substantially larger contrast is desirable.

Based on the common results for transverse resonance and cutoff properties of slab waveguides [22], one can derive conditions for the occurrence of specific resonances. At a given wavelength λ, a symmetric slab waveguide constituted by materials n_{g} and n_{b} supports TE modes of order m with angles $\theta_{\mathrm{crit}} < \theta_m < \theta_{\mathrm{max}}$, if its core thickness t is within the interval $t_m^{\mathrm{co}} < t < t_m^{\mathrm{crit}}$ with

$$
t_m^{\mathrm{co}} = \frac{m}{2}\lambda \bigg/ \sqrt{n_{\mathrm{g}}^2 - n_{\mathrm{b}}^2} \quad \text{and} \quad t_m^{\mathrm{crit}} = \frac{\lambda}{n_{\mathrm{b}}}\left(\frac{m}{2} + \frac{1}{\pi}\arctan\sqrt{n_{\mathrm{g}}^2/n_{\mathrm{b}}^2 - 2}\right) < \frac{\lambda}{n_{\mathrm{b}}}\frac{m+1}{2}, \tag{23}
$$

where t_m^{co} is the cutoff thickness for the mode of order m, while the the mode angle θ_m drops below θ_{crit} at the thickness t_m^{crit}. When attempting to design a device that shows a specific resonance $m_x \times m_z$ at wavelength λ, expressions (23), evaluated for $m = m_x$ and $t = W$ or for $m = m_z$ and $t = L$, respectively, restrict the admissible range for the geometric dimensions. Alternatively, Eqs. (23) can be arranged to establish limits

$$
n_{\mathrm{b}}\frac{W}{m_x + 1} < \frac{\lambda_{m_x, m_z}}{2} < \sqrt{n_{\mathrm{g}}^2 - n_{\mathrm{b}}^2}\frac{W}{m_x}, \qquad n_{\mathrm{b}}\frac{L}{m_z + 1} < \frac{\lambda_{m_x, m_z}}{2} < \sqrt{n_{\mathrm{g}}^2 - n_{\mathrm{b}}^2}\frac{L}{m_z}, \tag{24}
$$

for the wavelength λ_{m_x, m_z} associated with the single mode resonance $m_x \times m_z$ in a device with given geometry.

7 Examples for resonant configurations

Figures 10–12 illustrate the extremal field patterns of resonant structures that are designed in this way, uniformly for a vacuum wavelength of $1.55\,\mu\mathrm{m}$. Table 1 collects the corresponding geometrical parameters and the classifications of the resonances. The marker symbols included in the field plots and in the table indentify the configurations in Figure 9. Note that the gray levels have been scaled for each plot individually. In all cases the port waveguides are adjusted to be phase matched with the relevant cavity mode of highest order. The corresponding mode profile extends furthest in the background medium, thus enabling an effective coupling to the incoming light in the port channels.

Symbol	Mode order	$W/\,\mu$m	$L/\,\mu$m	$w/\,\mu$m	$g/\,\mu$m
○ (0)	$6 \times 20 + 8 \times 16$	2.524	5.738	0.112	0.450
□ (1)	$7 \times 22 + 9 \times 16$	2.524	6.902	0.068	0.480
☆ (2)	$6 \times 11 + 8 \times 9$	2.655	3.111	0.130	0.350
◇ (3)	$1 \times 3 + 3 \times 1$	0.810	0.810	0.035	0.490
▽ (4)	$2 \times 4 + 4 \times 2$	1.132	1.132	0.059	0.400
◁ (5)	$3 \times 5 + 5 \times 3$	1.451	1.451	0.073	0.400
△ (6)	$4 \times 6 + 6 \times 4$	1.772	1.772	0.083	0.320
▷ (7)	$10 \times 12 + 12 \times 10$	3.696	3.696	0.108	0.420
☆ (8)	8×13	2.524	4.682	0.112	0.450
☆ (9)	8×18	2.524	6.423	0.112	0.450

Table 1: Geometrical parameters and relevant mode orders for the resonances shown in Figures 3, 10, 11, and 12. The refractive indices of the guiding region and of the background are $n_{\mathrm{g}} = 3.40$ and $n_{\mathrm{b}} = 1.45$. All patterns are observed for the vacuum wavelength $\lambda = 1.55\,\mu\mathrm{m}$.

Figure 10 shows two more example for high quality bimodal resonances in large rectangular cavities. Various symmetries of the field inside the cavity can be realized: Configuration (0) (Figure 3) is symmetric with respect to both the horizontal and the vertical symmetry planes. Configuration (1) is symmetric with respect to the vertical plane, and antisymmetric with respect to the horizontal plane; these symmetries are reversed in
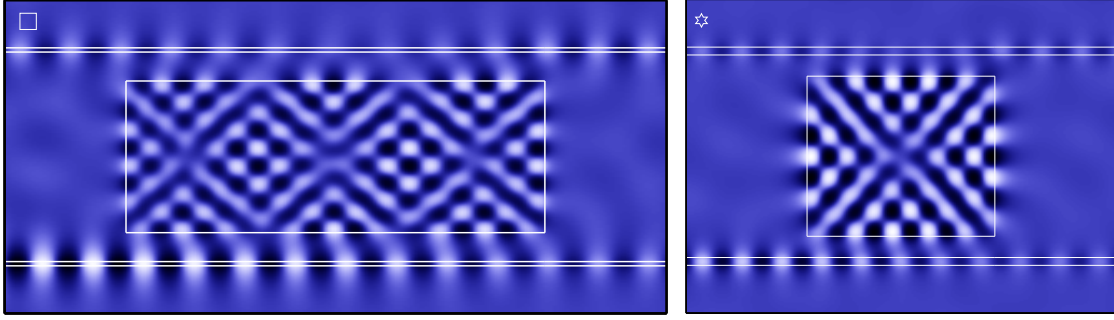
Figure 10: Field patterns of the bimodal resonances corresponding to the marker symbols in Figure 9 and Table 1, for the resonators (1) and (2) with rectangular cavities.

configuration (2). The orders of the relevant horizontal modes differ by 4, 6, and 2, for configurations (0), (1) and (2), respectively.

In the series of square cavities of Figure 11, the resonances in the smaller cavities are based on modes that are relatively close to the cutoff-angle, with a only moderate bimodal facet reflectivity (cf. Figures 9, 6). Consequently the cavity loss, the amount of radiation seen around the cavity, decreases with growing cavity size or with increasing order of the resonance, respectively.
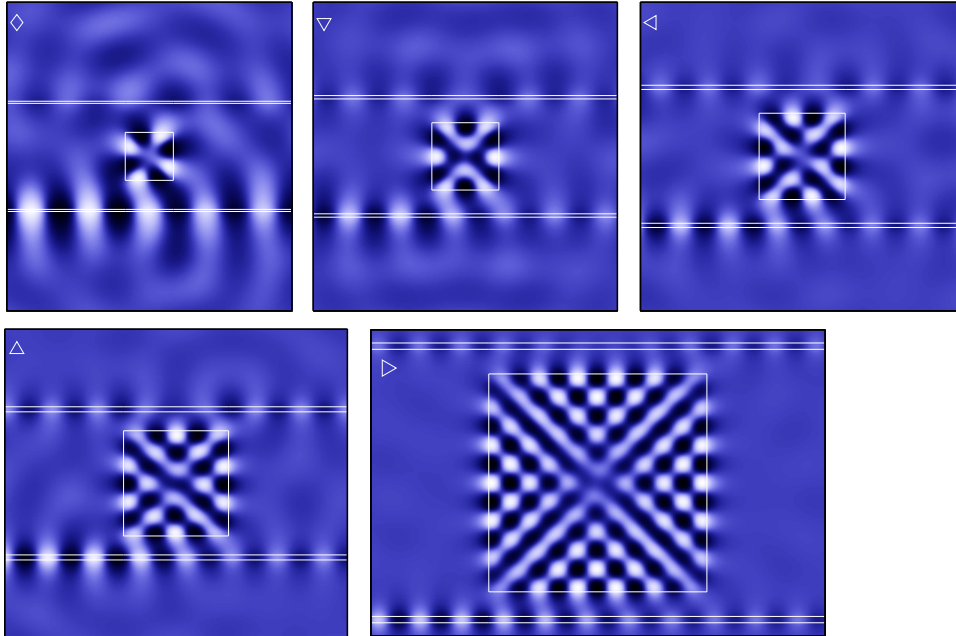

Figure 11: Field patterns of the bimodal resonances corresponding to the marker symbols in Figure 9 and Table 1, for the square cavity configurations (3) – (7).

Figure 12 shows the regular standing wave pattern of two single mode resonances. While the field strength at the cavity corners almost vanishes for the bimodal excitations of Figures 10, 11, the single mode resonances show a much larger field at these points. This leads to relatively large losses at the cavity facets with radiation patterns that resemble the cylindrical waves of Figure 7. Hence these resonances cause mainly a dip in the direct transmission P_{B}, without a large contribution to the power drop into the other resonator ports.

8   Conclusions

Supplemented by reflectivity matrices for the incidence of guided waves on facets of high contrast multimode slabs, we have applied a 2D coupled mode theory model to integrated optical microresonator devices, where a rectangular cavity connects two adjacent parallel waveguides. Comparison with rigorous mode expansion simulations led to a reasonable agreement. Being of a more approximate nature, where the high refractive
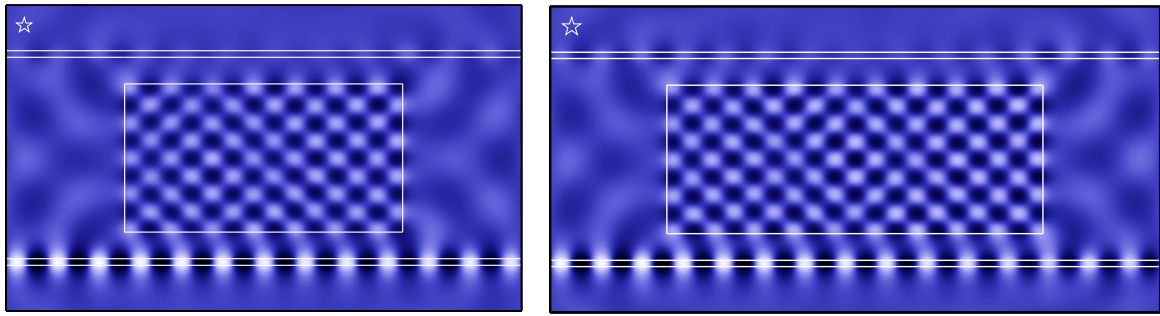
Figure 12: Field patterns for the single mode resonances marked in Figure 9, with parameters as given in Table 1, configurations (8) and (9).

index contrast and the long light path in a resonant configuration constitute somewhat extreme conditions, the coupled mode approach is nevertheless an ab-initio model without free parameters that gives some insight in the functional behaviour and proper design of the devices.

By means of the eigenvalues of the matrix denominator that appears in the coupled mode equations, the CMT model allows to identify the resonances associated with specific slab modes in isolated rectangular cavities. This concerns both the position and the quality of the excitations. The model predicts regularly appearing single mode resonances for modes with angles in a suitable range. A nearly total facet reflectivity as observed for mode superpositions with vanishing field at the cavity edges leads to more irregularly occurring bimodal resonances, that are of substantially higher quality in terms of losses to radiation and in terms of the amount of dropped power.

Resonant states in the rectangular cavities can be properly represented by guided slab modes. Applying this observation two times for mode propagation along the two cavity dimensions provides a means to determine device geometries which show a specific resonance at a prescribed vacuum wavelength. The procedure is based on the dependences of propagation constants or mode angles on the thickness of the slab waveguide cores. Although therefore explicit analytic expressions cannot be given, a common mode solver for symmetric single layer slab waveguides is in principle sufficient to predict resonant geometries, or resonance wavelengths, respectively, of the rectangular microresonators.

Perhaps an analogous reasoning can also be helpful when having to estimate whether reflections might play a significant role in waveguide segments with abrupt ends, as they are employed in — at a first glance quite similar — designs of e.g. multimode interference devices or integrated optical directional couplers. In an entirely different regime of parameters, the relatively stringent conditions concerning the geometry and the refractive index contrast will usually prevent that a waveguide segment forms a cavity, where resonance phenomena may become relevant.

Acknowledgment

References

[1] B. E. Little, S. T. Chu, W. Pan, and Y. Kokubun. Microring resonator arrays for VLSI photonics. *IEEE Photonics Technology Letters*, 12(3):323–325, 2000.

[2] Next-generation active integrated optic subsystems. Information society technologies programme of the European Commission, project IST-2000-28018, http://www.mesaplus.utwente.nl/nais/.

[3] D. J. W. Klunder, E. Krioukov, F. S. Tan, T. van der Veen, H. F. Bulthuis, G. Sengo, C. Otto, H. J. W. M. Hoekstra, and A. Driessen. Vertically and laterally waveguide-coupled cylindrical microresonators in Si_3N_4 on SiO_2 technology. *Applied Physics B*, 73:603–608, 2001.

[4] K. Djordjev, S.-J. Choi, S.-J. Choi, and P. D. Dapkus. Active semiconductor microdisk devices. *Journal of Lightwave Technology*, 20(1):105–113, 2002.

[5] E. A. J. Marcatili. Bends in optical dielectric guides. *The Bell System Technical Journal*, September:2103–2132, 1969.

[6] D. R. Rowland and J. D. Love. Evanescent wave coupling of whispering gallery modes of a dielectric cylinder. *IEE Proceedings, Pt. J*, 140(3):177–188, 1993.

[7] B. E. Little, S. T. Chu, H. A. Haus, J. Foresi, and J.-P. Laine. Microring resonator channel dropping filters. *Journal of Lightwave Technology*, 15(6):998–1005, 1997.

[8] M. K. Chin and S. T. Ho. Design and modeling of waveguide-coupled single-mode microring resonators. *Journal of Lightwave Technology*, 16(8):1433–1446, 1997.

[9] B. E. Little, J.-P. Laine, and H. A. Haus. Analytic theory of coupling from tapered fibers and half-blocks into microsphere resonators. *Journal of Lightwave Technology*, 17(4):704–715, 1999.

[10] S. V. Boriskina and A. I. Nosich. Radiation and absorption losses of the whispering-gallery-mode dielectric resonators excited by a dielectric waveguide. *IEEE Transactions on Microwave Theory and Techniques*, 47(2):224–231, 1999.

[11] S. V. Boriskina, T. M. Benson, P. Sewell, and A. I. Nosich. Effect of a layered environment on the complex natural frequencies of two-dimensional WG-mode dielectric ring resonators. *Journal of Lightwave Technology*, 2001. (Submitted).

[12] J. U. Nöckel and A. D. Stone. Ray and wave chaos in asymmetric resonant optical cavities. *Nature*, 385:45–47, 1997.

[13] E. Gornik. Geometrical shaping of microlaser emission patterns. *Science*, 280:1544–1545, 1998.

[14] C. Manolatou, M. J. Khan, S. Fan, P. R. Villeneuve, H. A. Haus, and J. D. Joannopoulos. Coupling of modes analysis of resonant channel add-drop filters. *IEEE Journal of Quantum Electronics*, 35(9):1322–1331, 1999.

[15] A. I. Nosich and S. V. Boriskina. Fast solution to the scattering by arbitrary smooth dielectric cylinders based on the method of regularization. *Proceedings of the International Conference on Transparent Optical Networks (ICTON 2000), Gdansk, Poland*, pages 27–30, 2000.

[16] M. Lohmeyer. Mode expansion modeling of rectangular integrated optical microresonators. *Optical and Quantum Electronics*, 34(5):541–557, 2002.

[17] A. Haus and C. G. Fonstad. Three-waveguide couplers for improved sampling and filtering. *IEEE Journal of Quantum Electronics*, 17(12):2321–2325, 1981.

[18] J. P. Donelly. Limitations on power transfer efficiency in three-guide optical couplers. *IEEE Journal of Quantum Electronics*, 22(5):610–616, 1986.

[19] K. L. Chen and S. Wang. The crosstalk in three-waveguide optical directional couplers. *IEEE Journal of Quantum Electronics*, 22(7):1039–1041, 1986.

[20] M. Shamonin, M. Lohmeyer, and P. Hertel. Directional coupler based on radiatively coupled waveguides. *Applied Optics*, 36(3):635–641, 1997.

[21] M. Lohmeyer, N. Bahlmann, O. Zhuromskyy, and P. Hertel. Radiatively coupled waveguide polarization splitter simulated by wave-matching based coupled mode theory. *Optical and Quantum Electronics*, 31:877–891, 1999.

[22] C. Vassallo. *Optical Waveguide Concepts*. Elsevier, Amsterdam, 1991.

[23] D. G. Hall and B. J. Thompson, editors. *Selected Papers on Coupled-Mode Theory in Guided-Wave Optics*, volume MS 84 of *SPIE Milestone Series*. SPIE Optical Engineering Press, Bellingham, Washington USA, 1993.

[24] M. Hammer and E. van Groesen. Total multimode reflection at facets of planar high contrast optical waveguides. *Journal of Lightwave Technology*, 2002. (Accepted).

[25] G. Sztefka and H. P. Nolting. Bidirectional eigenmode propagation for large refractive index steps. *IEEE Photonics Technology Letters*, 5(5):554–557, 1993.

[26] M. Lohmeyer and R. Stoffer. Integrated optical cross strip polarizer concept. *Optical and Quantum Electronics*, 33(4/5):413–431, 2001.